Surface-Enhanced Raman Spectroscopy Based on Plasmonic Slot Waveguides With Free-Space Oblique Illumination

Yang Li, Haolan Zhao, Ali Raza, Stéphane Clemmen, and Roel Baets, *Fellow, IEEE*

***Abstract*— We report a novel on-chip approach for surface-enhanced Raman spectroscopy (SERS) using a plasmonic slot waveguide. The Raman signal is excited via free-space excitation and is collected by the waveguide. A significant improvement of the signal-to-background-ratio (SBR), as compared to the case of back-scattered Raman spectroscopy with waveguide-mode excitation, is demonstrated using a silicon nitride plasmonic slot waveguide with a 7-mm access waveguide. The flexible adjustment of the incident angle in free space and modification of waveguide geometry enables the further optimization of the pump-to-Stokes conversion efficiency. The combination of high SBR and long access waveguide allows the integration with additional photonics devices (sources, filters, spectrometers) on the same chip.**

***Index Terms*— Free-space excitation, integrated optics, on-chip sensors, plasmonic slot waveguide, surface-enhanced Raman spectroscopy.**

I. Introduction

RAMAN spectroscopy has the capability of identifying molecular fingerprints [1]–[3]. It has been widely used as a powerful spectroscopic technique in various fields ranging from biology, chemistry to material science [4], [5]. However, most materials have a very small Raman cross-section, leading to extremely weak signals. The inherent weakness of Raman signals has precluded Raman spectroscopy from ultra-sensitive applications. This problem has been greatly alleviated by the discovery of surface-enhanced Raman scattering (SERS), which relies on a strong local-field enhancement capable of intensifying the electric field by many orders of magnitudes. The conventional SERS substrates such as metal nanoparticles [6], [7], gold nanowire [8] and other nano-patterned structure [9]–[11] are typically relying on an off-chip confocal Raman microscope that is bulky and costly. As a result, applications of SERS are mainly confined to laboratory settings.

More recently, nanophotonic waveguides have emerged as effective means to enhance spontaneous Raman signals. In this case, the evanescent tail of a guided mode is used to efficiently excite and collect a Raman signal. Since the optical excitation is tightly confined by the waveguide, the interaction length is significantly increased, resulting in a vast enhancement of the Raman signal. Spontaneous Raman spectroscopy on silicon nitride waveguides has been demonstrated to detect bulk liquid of isopropyl alcohol [12] and biological monolayers [13].

To further enhance the Raman signal intensity, the hybrid integration of nanophotonic waveguides with plasmonic structures has been proposed to leverage both the waveguide enhancement and the strong field enhancement [14]–[17]. This idea has been explored by introducing nanoplasmonic antennas and microspheres onto the top surface of dielectric waveguides. In those structures however, the optical field are mostly confined within the Si_3N_4 waveguide core and this gives rise to a strong spurious Raman background. The spectrum of this background being itself a function of the mode shape, it depends slightly on the optical cladding (analyte) and therefore cannot be known perfectly for an unknown analyte. Moreover, the shot-noise associated with this background cannot be subtracted and constitute the greatest limiting factor to the signal-to-noise ratio [18]. The impact of this background is therefore detrimental [18]–[20], and its reduction has a high impact on the future prospects of on-chip Raman sensing.

To suppress the Raman background, a later study made use of an ALD-assisted metallic slot waveguide, where the optical field is confined tightly in the analyte, instead of the waveguide core [21]–[24]. The remaining bottleneck of that demonstration concerns its integration with spectrometer and on-chip detectors. It has been shown that 100-μm-short access waveguide preceding the metallic slot waveguides had a significant impact on the signal-to-background ratio, leaving little room to integrate other photonic components, such as pump filters and input tapers.

Here, we report a new experimental configuration of plasmonic slot waveguides for monolayer sensing, where the

Manuscript received June 26, 2019; revised September 12, 2019; accepted October 2, 2019. Date of publication October 10, 2019; date of current version November 21, 2019. This work was supported in part by the Fonds Wetenschappelijk Onderzoek (FWO) Belgium and in part by the National Natural Science Foundation of China under Grant 61535010. The work of Y. Li was supported by the China Scholarship Council. S. Clemmen is a Research Associate of the Fonds de la Recherche Scientifique (FNRS). *(Corresponding author: Yang Li.)*

Y. Li is with the State Key Laboratory of Modern Optical Instrumentation, College of Optical Science and Engineering, Zhejiang University, Hangzhou 310007, China, and also with the Photonics Research Group, Ghent University–IMEC and Center of Nano- and Biophotonics (NB-Photonics), Ghent University, Ghent 9000, Belgium (e-mail: yang.li@ugent.be).

H. Zhao, A. Raza, and R. Baets are with the Photonics Research Group, Ghent University–IMEC and Center of Nano- and Biophotonics (NB-Photonics), Ghent University, Ghent 9000, Belgium (e-mail: haolan.zhao@ugent.be; ali.raza@ugent.be; roel.baets@ugent.be).

S. Clemmen is with the Photonics Research Group, Ghent University–IMEC and Center of Nano- and Biophotonics (NB-Photonics), Ghent University, Ghent 9000, Belgium, with the Laboratoire d'Information Quantique, Université Libre de Bruxelles, 1000 Brussels, Belgium, and also with OPERA-Photonique, Université Libre de Bruxelles, 1000 Brussels, Belgium (e-mail: stephane.clemmen@ugent.be).

Color versions of one or more of the figures in this article are available online at http://ieeexplore.ieee.org.

Digital Object Identifier 10.1109/JQE.2019.2946839

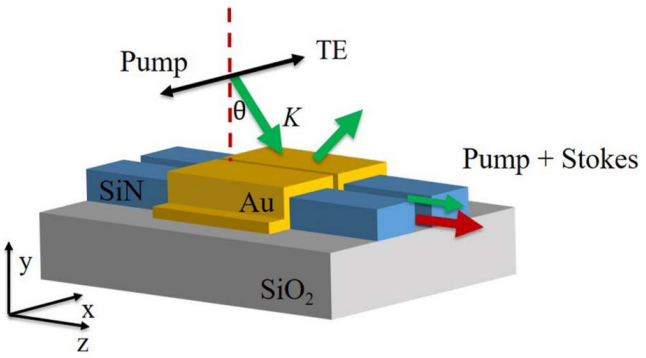

Fig. 1. The schematic of plasmonic slot waveguide with oblique illumination in free space. The red dashed line is perpendicular to the top surface of the waveguide. The green and the red arrows indicate the propagation directions of the pump beam and Stokes beam respectively.

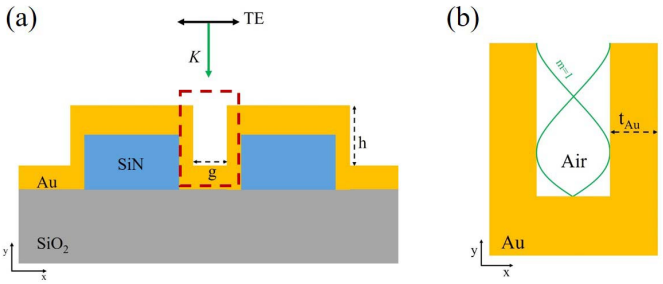

Fig. 2. (a) Cross-section of the plasmonic slot waveguide under the illumination of TE-polarized pump beam from top. The enhanced excitation field is generated in the gap, which is highlighted by the red dashed rectangle. (b) A zoom-in view of the red dashed area in Fig. 2(a). The SPP is in resonance within the gap with an antinode on the gold end and a node on the open end.

plasmonic structure is excited from the top in free-space and the Raman signal is collected by the waveguide. Unlike the traditional SERS substrates that operate in free-space excitation and collection, our configuration allows the integration with many photonic components (i.e. filters, spectrometers) on a small chip. This will reduce the size and cost of the SERS device. Our approach provides a considerable improvement in the signal-to-background ratio (SBR) for plasmonic slot waveguides having a 7-mm long access waveguide. In addition, there is a negligible coupling of the pump beam from free-space to the waveguide mode. It not only ensures negligible Raman background, but it also provides a 50 dB pump rejection in effect. The latter alleviates the burden of integrated pump rejection filter, allowing an all-on-a-chip integration.

II. Physical Theory

Fig. 1 shows the geometric scheme of our demonstration. A pump beam with an x-polarized electric field (we also call it TE-polarized) is obliquely incident from free space to the top surface of the gold-coated slot waveguide via an objective. The focal spot is located at the center of the plasmonic slot waveguide. The pump wavelength is set to $\lambda_p = 785$ nm. The sample is functionalized with 4-nitrothiophenol (NTP) ethanol solution. The gold is coated with an NTP monolayer. The NTP molecules are excited and radiate Stokes light (at λ_s), which is coupled to the fundamental plasmonic mode of the gold-coated slot waveguide. Both the Stokes light and a small fraction of the pump light are subsequently collected into the dielectric slot waveguide mode, thanks to the overlap between the plasmonic mode and the dielectric waveguide mode. The excitation and the collection processes are introduced below.

A. Free-Space Excitation

Fig. 2(a) shows the cross-section of the plasmonic slot waveguide illuminated from free-space and Fig. 2(b) shows a zoom-in view of the gold-air-gold structure which is marked by the dashed rectangle in Fig. 2(a). The gold-air-gold configuration can be modeled as a metal-dielectric-metal (MDM) structure, which has been well studied in plasmonics. As predicted by Maxwell's equations, the incident pump excites a symmetric surface plasmon-polariton (SPP) mode within the gap. After reaching the bottom gold layer, the SPP reflects. The characteristic propagation length of SPP is in the range of 1-10 μm, which is much longer than the depth of the gap. As a result, the reflected SPP has a similar strength as the incident SPP mode, and the gold-air-gold structure can be regarded as a cavity terminated by air on the top and gold end on the bottom. If the SPP resonates in the cavity, the electric field within the gap is significantly amplified, leading to an enhanced Raman signal. The resonance condition is given by

$$hk_{spp}(\lambda_p, g) = \pi\left(m + \frac{1}{2}\right). \quad (1)$$

Here, m is the order of resonance, h is the height of the air gap, and $k_{spp}(\lambda_p)$ is the wave-vector of the SPP, which is determined by the width g and the pump wavelength λ_p. Since the local field enhancement is maximized for the lowest order resonant mode, the target is to find a configuration that satisfies (1) with $m = 1$.

The pump wavelength in our demonstrations is fixed to 785 nm. To satisfy the resonance condition, we can only adjust the geometry of the waveguide. Since the width of the gap g is closely related to the obtainable field enhancement factor, in practice we keep g below 80 nm for sufficient electric field enhancement.

However, our study shows that the resonance condition requires the slot height h to be lower than 100 nm, which is not compatible with the dielectric slot waveguide to which the plasmonic slot is coupled. Fortunately, the resonance condition is only relevant to the wave-vector along the y-direction. It suggests we can satisfy the resonance condition by oblique incidence as shown in Fig. 1. The pump beam is injected into the gold-air-gold structure with an angle of θ relative to the y axis. The new resonance condition is given by

$$hk_{spp}(\lambda_p, g)\cos\theta = \pi\left(m + \frac{1}{2}\right). \quad (2)$$

B. Waveguide-Mode Collection

Once the SPP pump field is excited, the confined pump field excites the vibrational modes of the NTP molecules, which can be viewed as radiating dipoles. The NTP molecules are coated as a uniform monolayer on the gold surface. These excited

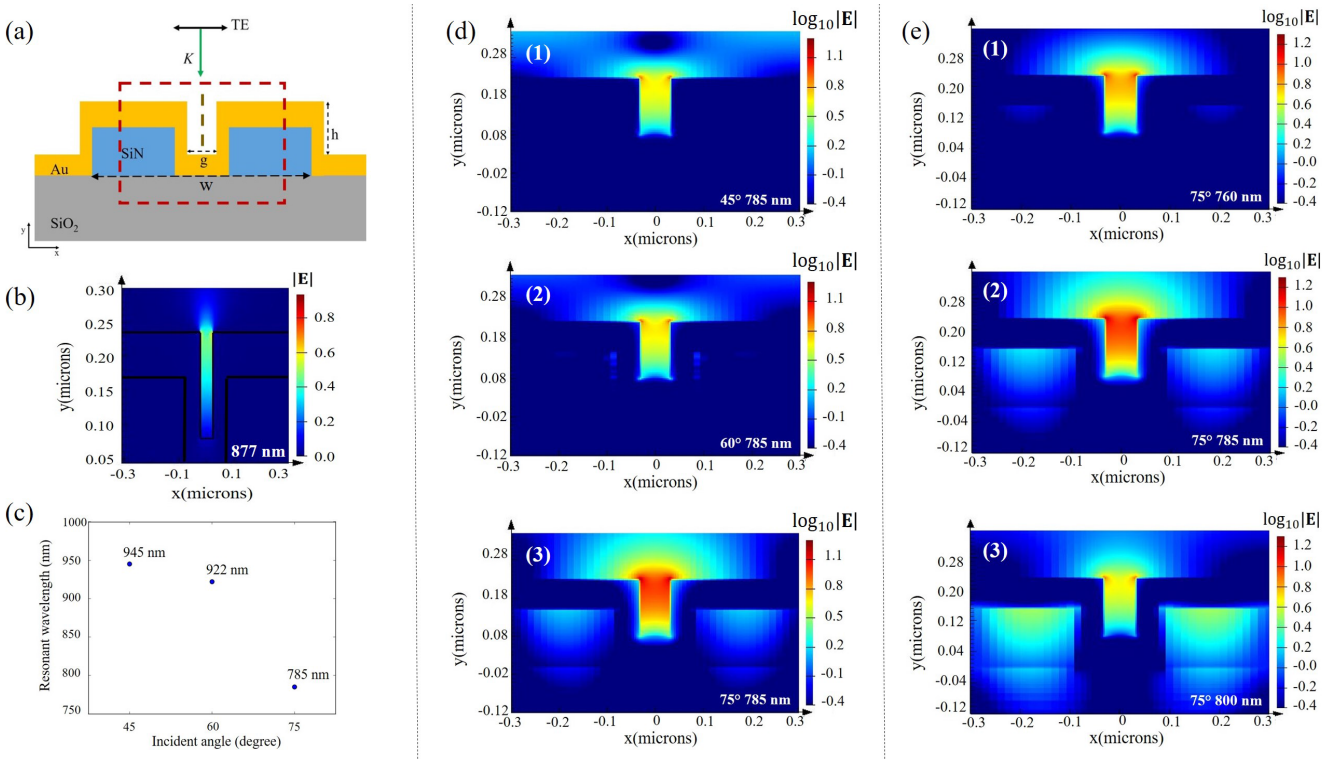

Fig. 3. (a) The cross section of the simulation model. The green dashed line is a 1D monitor for electric field and power. The red dashed box is a 2D monitor for electric field and power. (b) The strength distribution of the fundamental TE mode of the plasmonic slot waveguide at 877 nm. (c) The resonant wavelengths from the simulations with different incident angles and other dimensions fixed ($w = 1200$ nm, $g = 65$ nm, $h = 150$ nm). (d) The Electric field strength distributions of for excitation at incident angles of 45° (1), 60° (2), and 75° (3) assuming a pump wavelength of 785 nm. (e) The Electric field strength distributions for an excitation at a pump wavelengths of 760 nm (1), 785 nm (2), 800 nm (3) assuming an incident angle of 75°. Note that (d) 3 and (e) 2 are the same plot.

dipoles emit a Stokes signal, and the major part of it couples to the propagation mode of the gold-coated slot waveguide, which propagates along the z-direction, as shown in Fig. 1.

The plasmonic slot waveguide mode then is coupled into the fundamental mode of the dielectric slot waveguide which is later converted to dielectric strip waveguides with dedicated couplers. At the end of the dielectric strip waveguide, the Stokes signal is collected by an objective and sent to a spectrometer for analysis. It is worth noting that the SPP pump beam can also couple to the guided mode. However, the coupling efficiency is as low as −50 dB so that we can safely ignore the Raman background generated at the exit waveguide.

III. Simulation

To verify the analytical formula depicted in (2), we simulate the structure with Lumerical FDTD solver. Based on the simulation results, the overall conversion efficiency [24], [25] is calculated.

A. Configurations of the Simulation

We consider a Si_3N_4 slot waveguide coated with a gold layer. The refractive indices of the Si_3N_4 and the gold are estimated from respectively Philip model and Johnson and Christy model in the material library of Lumerical. The cross-section of the plasmonic slot waveguide is shown in Fig. 3(a). The input field is approximated as a plane wave with an electric field of 1 V/m. The plane wave is TE-polarized and is incident on the plasmonic slot waveguide with an angle θ, which is not marked in Fig. 3(a). The width of the waveguide w is 1200 nm and the height h is 150 nm. The thickness of the gold along the sidewall in the gap t_{Au}(marked in Fig. 2(b)) is 15 nm. We swept the gap width g and the source wavelength from 500 nm to 1500 nm under different incident angles (45°, 60°,75°). We place a line monitor (the green dashed line in Fig. 3(a)) in the center of the gap to get the electric field distribution along the central line. We know from previous section that the Raman signal (λ_s) produced in the resonant electric field must couple to the fundamental mode of the plasmonic slot waveguide, the strength distribution of which is showed in Fig. 3(b). The Electric field strength distribution is simulated via Lumerical Mode Solution. The wavelength in Fig. 3(b) is set to 877 nm, which is the main Raman peak wavelength of the analyte in our demonstration. Then the Raman signal propagates along the plasmonic waveguide as well as the Si_3N_4 waveguides to the output port of the sample. For specified gap width and incident angle, the strength of the electric field is maximized when the pump beam is in resonance with the cavity. Fig. 3(c) shows the resonant wavelength for various incident angles with a gap width of $g = 65$ nm. The resonant wavelength is blue-shifted as the angle increases, which is consistent with (2).

To further investigate the enhancement effect due to the resonance, a 2D monitor (the red dotted box in Fig. 3(a)) is placed to get the electric field distribution. We simulate the excitation electric field distribution at various incident angles

($\theta = 45°, 60°, 75°$) when the gap width is 65 nm and the pump wavelength is 785 nm. This wavelength is in resonance with the cavity at 75° incidence. The results are shown in Fig. 3(d). The strength enhancement of the excitation Electric field with 75-degree illumination is stronger than those with 45-degree and 60-degree incident angles. In our simulation, we approximate the input pump beam as a plane wave. The pump intensity on the top surface of the plasmonic waveguide varies as a cosine of the incidence angle. This means the excitation field generated by a 75-degree incidence has the maximum Electric field strength enhancement despite the pump intensity at 75 degrees being less than 60 degrees and 45 degrees.

The incident angle and the gap width of the plasmonic structure are optimized to make the pump light at $\lambda_p = 785$nm resonate in the slot. If we change this wavelength by more than 10 nm, we can see (Fig. 3(e)) the field enhancement is significantly reduced and is even more reduced at the Raman wavelength $\lambda_s = 877$nm.

B. Evaluation of the Total Raman Conversion Efficiency

To compare the performance of both waveguide excitation and free space excitation, it is critical to estimate the conversion efficiency of both methods based on the same waveguide dimensions. Here we define the Raman conversion efficiency as the ratio of the Stokes power coupled into the waveguide mode over the input pump power. For waveguide excitation, the conversion efficiency for the NTP Stokes peak of 1340 cm^{-1} is 10^{-10} [25] when the pump wavelength λ_p is 785 nm and the Stokes wavelength λ_s is 877 nm.

To estimate the conversion efficiency, we proceed as follow. First, we approximate the Raman emitter (NTP) as a dipole source oscillating at the Stokes frequency. The power radiated by a dipole in a homogeneous medium with index n is given by

$$P_0 = \frac{4\pi^3 cn\,|\mathbf{d}|^2}{3\epsilon_0 \lambda_s^4} \tag{3}$$

here c is light velocity in vacuum, λ_s is the Stokes wavelength and $\mathbf{d}$ is the dipole moment which is given by the formulas:

$$|\mathbf{d}|^2 = \alpha^2 \left|\mathbf{E}_{ex}(\mathbf{r}_e, \lambda_p)\right|^2 \tag{4}$$

$$\alpha^2 = \frac{\sigma \epsilon_0^2 \lambda_s^4}{\pi^2} \tag{5}$$

here α is the Raman transition polarizability which is associated to the Raman scattering cross section σ by (5). $\mathbf{E}_{ex}$ is the excitation electric field generated by the pump field at the wavelength of λ_p and $\mathbf{r}_e$ is the position of the dipole.

The Raman cross section σ for NTP is $1.8\times10^{-29}$$cm^2$/sr. Fig. 3d (3) presents the amplitude of the Electric field at λ_p assuming an oblique plane wave excitation at 75° with an electric field of 1 V/m. From this distribution, we can calculate the Raman power P_0 radiated by an emitter located at $\mathbf{r}_e$ in a homogenous medium with the index n. A fraction of this power (P_{wg}) will be coupled to the forward propagating mode of the waveguide. The coupling efficiency between P_{wg} and P_0 is given by [12]:

$$\frac{P_{wg}(\mathbf{r}_e)}{P_0} = \frac{3}{8\pi}\frac{n_g(\lambda_s)}{n}\left(\frac{\lambda_s}{n}\right)^2 \frac{\varepsilon(\mathbf{r}_e)\,|\mathbf{d}_0 \cdot \mathbf{E}(\mathbf{r}_e, \lambda_s)|^2}{\iint \varepsilon_0 \varepsilon(\mathbf{r})\,|\mathbf{E}(\mathbf{r}, \lambda_s)|^2\,d\mathbf{r}}. \tag{6}$$

here n_g is the group index of the plasmonic fundamental mode. n is the refractive index of the medium where the molecule is located. $\varepsilon(\mathbf{r})$ is the relative permittivity. $\mathbf{d}_0$ is the unit dipole moment and $\mathbf{E}(\mathbf{r}, \lambda_s)$ is the electric field distribution of the fundamental mode of the plasmonic slot waveguide which can be calculated through Lumerical Mode Solution setting the source wavelength to λ_s. Fig. 3(b) shows the field strength distribution of the propagating mode at λ_s. The integration in the denominator of (6) runs over the complete plasmonic waveguide cross section (including the optical cladding).

In the present case, the cladding is a 1nm-thick layer of NTP that selectively binds to gold. We assume that the NTP molecules are uniformly bond to gold with a molecular density of 4.4×10^6 molecules/μm^2 [24]. The total Raman conversion efficiency of free-space excitation is estimated to be 5.5×10^{-11}, which is one order of magnitude lower than that of waveguide excitation. However, it is worthwhile to point out that this conversion efficiency is calculated based on available samples in our lab whose height is fixed to 150 nm. The efficiency can be greatly improved by adjusting the gap height and width of the plasmonic slot waveguide but requires dedicated Si_3N_4 waveguides with the proper thickness. For instance, the conversion efficiency can be ten times higher than the current value when the height of the gap is 110 nm, the gap width is 35 nm and the incident angle is 60°.

IV. Fabrication

The plasmonic slot waveguide is fabricated on a 150-nm-thick plasma-enhanced chemical vapor deposition (PECVD) Si_3N_4 wafer. The silicon nitride is deposited on top of a 3-μm-thick layer of PECVD silicon dioxide.

Firstly, we spin-coat a layer of electron beam (E-beam) lithography photoresist (ARP 09) on the wafer and transfer the structure pattern to the sample by E-beam exposure. The sample is soaked in developer (n-Amy acetate) for 1 minute and is later rinsed with isopropanol. The development is followed by 10-second oxygen plasma to strip the residual resist. Then we etch the sample with reactive ion etching (RIE). On average, the dielectric waveguide is about 1.2 μm wide with a 80-100 nm slot. The etching depth is in the range of 150-160 nm. After the fabrication of the Si_3N_4 slot waveguide, we spin coat a layer of photolithography photoresist (AZ 5214) on the sample to transfer the pattern of the plasmonic structure via contact photolithography. Before the metallic depositions, the sample is treated with oxygen plasma for 30 s to remove possible remaining resist. Then a 1-2 nm thick Ti adhesion layer and a 15-20 nm thick Au layer are deposited on the sample consecutively with a sputtering machine. In the step of gold deposition, we ensure the thickness of gold at side wall of the waveguide is within 15-20 nm.

The fabrication of our plasmonic slot waveguide is finished after a gold lift-off. The whole process is summarized

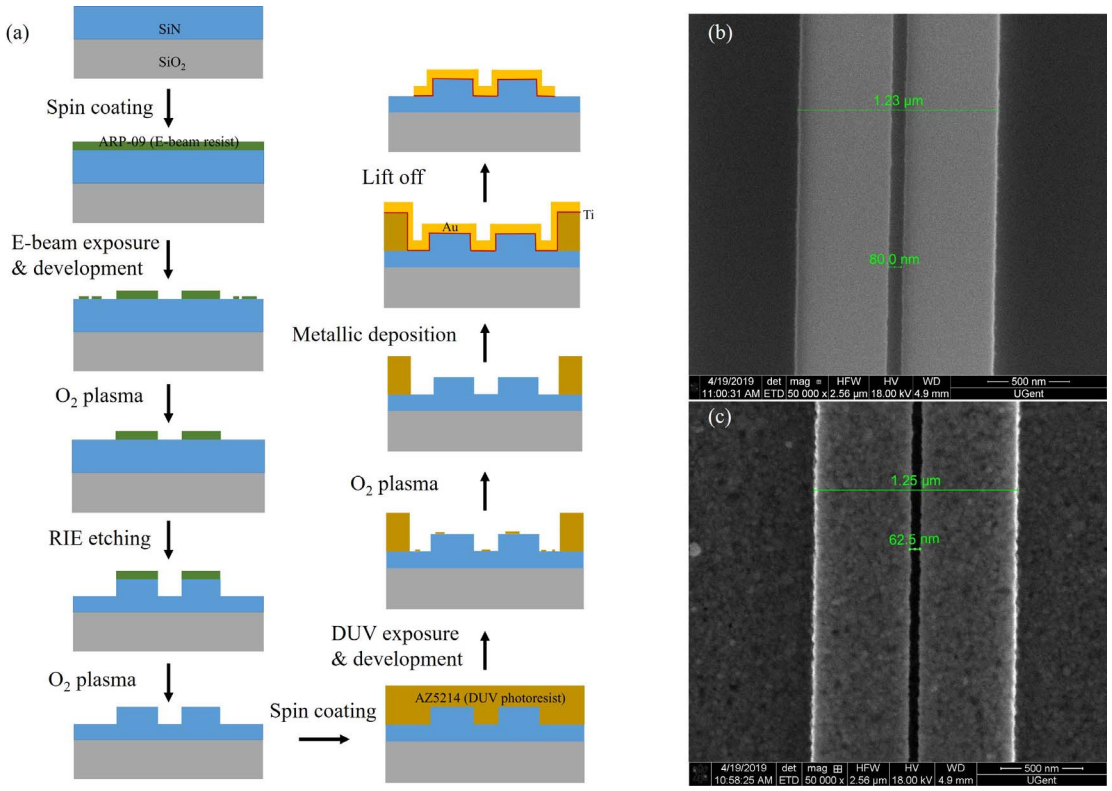

Fig. 4. (a) Flow diagram of the sample fabrication. (b) SEM image of the silicon nitride slot waveguide. (c) SEM image of the gold-coated plasmonic slot waveguide.

in Fig. 4 The plasmonic slot waveguide is then functionalized with a monolayer of 4-nitrothiophenol (NTP) for characterization. We clean the sample with oxygen plasma after rinsing it with acetone, isopropanol and deionized water. Then the sample is immersed in NTP ethanol solution for at least 3 hours so that the NTP molecules bind to the gold surface of the plasmonic slot waveguide.

V. Experimental Setup and Results

A. Measurement Setup

The free-space oblique excitation measurement setup is illustrated in Fig. 5(a). A Ti:Sapphire laser (Solstis, M-Squared) emitting at $\lambda_p = 785$ nm is used as the pump source (red). The pump laser is collimated in the free-space through a fiber collimator. A polarizer is installed to ensure the TE polarization of the pump, and a laser line filter is employed to clean the spectrum of pump beam. Then the pump beam is focused onto the plasmonic waveguide with an objective (Nikon, 50X, NA=0.6). The fiber collimator, polarizer, line filter and objective are mounted on a plate with adjustable angle.

The Stokes beam (green) is collected with another objective (50×, NA=0.65). Then it passes through a dichroic mirror which reflects the light at a wavelength below 800 nm while transmitting the light above 800 nm therefore removing the remaining pump beam. The Stokes beam is then collected via a multimode fiber (MMF) with a parabolic mirror collimator (PMC). The multimode fiber is connected to a commercial spectrometer (Shamrock 303i spectrometer and Andor iDus 416 deep-cooled CCD camera).

An important advantage of this new Raman sensor against previous ones is the large extinction of the pump beam. Indeed, a lower pump beam implies a strongly reduced background due to Si_3N_4.

To illustrate the significant reduction of the Si_3N_4 background, we can compare the performances of the Raman sensor when excited via the waveguide versus an excitation via the angled free-space illumination configuration. In Fig. 5(b), we show the measurement set up used to excite the Raman signal via the waveguide rather than from top. The pump light (λ_p) from the Ti:Sapphire laser is brought to the setup via a fiber collimator and goes through the same laser line filter and polarizer as in the free-space excitation setup. The TE-polarized pump reaches a dichroic mirror through three reflectors (R). We use the same objective to inject the pump light into the sample and to collect the output Raman spectrum from it. The Raman signal is separated from the residual monochromatic pump by the dichroic mirror. All the optics between the dichroic mirror and the spectrometer are identical in both the free-space excitation set up and the waveguide excited one.

To understand better the details of both configurations, a closer look at the structure can be taken by looking at Fig. 5(c). The structure in blue is the Si_3N_4 waveguide. It is composed of five sections: a slot waveguide, a taper between slot waveguide to strip waveguide, a strip waveguide, a taper from strip waveguide to edge coupler, and an edge coupler. Gold is deposited on the slot waveguide section (yellow rectangle) to make it a plasmonic slot waveguide. In the free-space excitation, the pump is injected into the

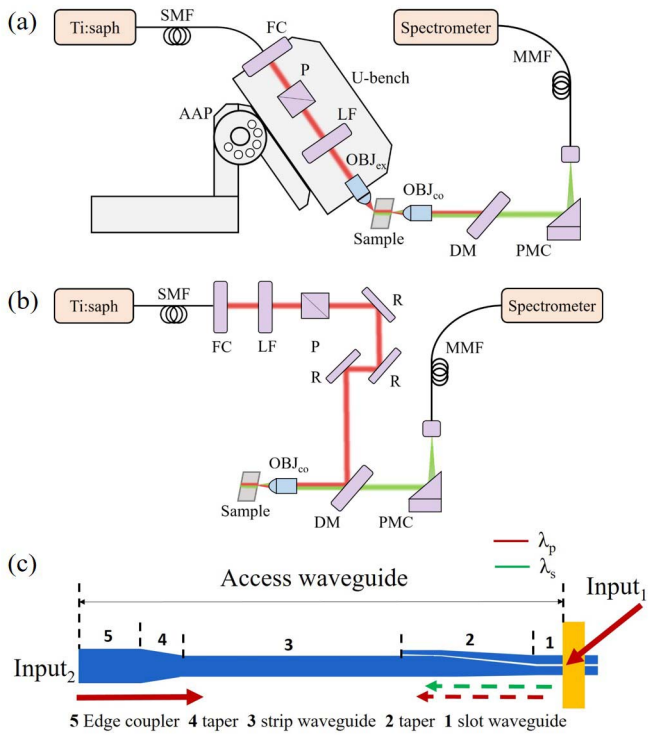

Fig. 5. (a) The schematic diagram of the free-space excitation experimental setup. Ti:saph: tunable Ti:sapphire laser, SMF: single mode fiber, FC: fiber collimator, P: polarizer, LF: line filter to clean the pump beam, OBJ_{ex}: objective (50×, NA=0.6) for free-space excitation, AAP: adjustable angle plate, OBJ_{co}: objective (50×, NA=0.65) for signal collection, DM: dichroic mirror, PMC: parabolic mirror collimator, MMF: multimode fiber. (b) The schematic diagram of the waveguide-mode excitation measurement set up. R: reflector. (c) Our Raman plasmonic sensor (yellow) complemented by a Si_3N_4 mode converter between slot and strip waveguides, a strip waveguide and a taper for in/out coupling to free space.

sample from $Input_1$. In the waveguide-mode excitation, pump beam is injected from $Input_2$. For waveguide-mode excitation, the whole waveguide from input facet to the plasmonic slot waveguide is defined as the access waveguide. We measure the same sample with the two excitation methods and detail the results hereafter.

B. Experiments With Free-Space Excitation

The waveguides in our samples have a nominal cross-section of 150 × 1250 nm^2 with a gap of 150 × 65 nm^2. The gold surface of the waveguide is coated with a monolayer NTP. Illuminating the waveguide with a 75-degree incident pump beam, we can clearly observe the emergence of three NTP peaks (1108 cm^{-1},1340 cm^{-1}, 1560 cm^{-1}) as shown in Fig. 6(a).

To gain a deeper understanding of the plasmonic resonance, we investigate the dependence of the Raman signal on the incident angle. We gradually reduce the incidence angle to 60°, 45°. The Raman spectra of the NTP functionalized waveguide at varying incident angles are shown in Fig. 6(a). For different incident angle, the input power before the objective is fixed at 1 mW. Moreover, the spectra in Fig. 6(a) are normalized by the cosine of the incident angle. The expected NTP peaks are highlighted with the blue shaded areas. It is clear that the Raman signal gets smaller with reduced incident angle in the case of the same pump intensity.

To understand the difference between the electric field enhancement caused by varying incident angles, it is critical to estimate the signal conversion efficiency of each angle. Taking into account the coupling loss from the chip facet to the detector (12-14 dB) and the efficiency of the spectrometer, we estimate the Raman conversion efficiency of the Stokes Raman resonance at 1340 cm^{-1} at each incidence angle and compared them in Fig. 6(b). The overall Raman conversion efficiency reduces with incident angle, which is consistent with the theory. It indicates that the dimensions of the plasmonic slot waveguide satisfy the resonance condition and we obtain the maximum local field enhancement at 75° incidence.

The Raman signal intensity in Fig. 6(a) and the Raman conversion efficiency in Fig. 6(b) both reveal that the performance of the Raman sensor with 75° illumination is more efficient than those with other incident angles. This is also indicated in the simulation results of Fig. 3(c), which shows that the pump wavelength 785 nm can resonate in the slot of the plasmonic waveguide at 75° incident angle based on the experimental waveguide dimensions. Besides, the simulated Electric field strength at different incident angles in Fig. 3(d) presents an enhancement decreasing with the angle in the same way as the Raman signal intensity in Fig. 6(a) and the Raman conversion efficiency in Fig. 6(b). It shows the important role of the angle of incidence on the resonant enhancement provided by the plasmonic structure.

In our experiments, we find that the Raman signal intensity is sensitive to the alignment in the z-direction (refer to the coordinate system in Fig. 1). We measure a Raman spectrum every ∼100 nm along the z-direction starting from the position where the NTP Stokes peaks emerge. This is done for 75° incidence angle and we consider the 1340 nm^{-1} Raman peak. The result plotted in Fig. 6(c) shows that the signal strength first rises as the overlap between the beam spot and the plasmonic slot waveguide increases. Then it falls due to the propagation loss of the plasmonic waveguide mode.

C. Comparison Between Free-Space Excitation and Waveguide-Mode Excitation

One major benefit of replacing waveguide-excitation with free-space excitation is the resulting background suppression. Because there is no access waveguide in this free-space excitation, the Raman background generated by the silicon nitride waveguide core is expected to be negligible. To demonstrate the background suppression, we record the Raman signal excited by the guided mode using the same waveguides, and the result is shown in Fig. 6(d). The input power of both excitation methods is normalized to 1 mW. First, it appears that the Raman peak is slightly stronger in the case of a waveguide excitation. It is worth reminding that the current waveguide design is far from optimal. As we mentioned in the previous section, we can enhance the strength of the resonant Electric field by optimizing the height and the width of the gap. The higher Raman conversion efficiency is achievable with smaller gap size. More importantly, the fig. 6(d) shows that the

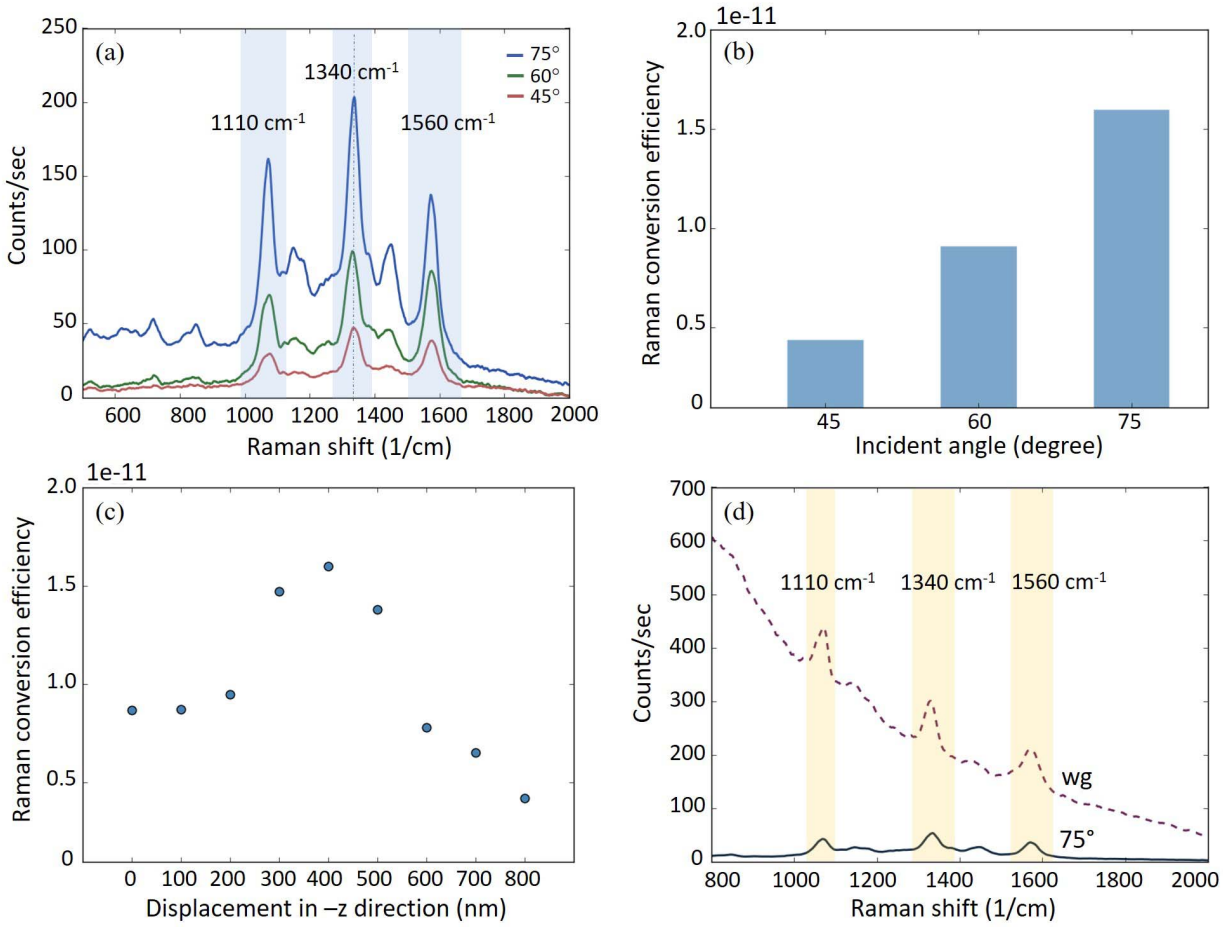

Fig. 6. (a) The measured Stokes signals of a NTP functionalized plasmonic slot waveguide with free-space oblique illumination. The incident angles are 45° (red), 60° (green), 75° (blue), respectively. The shaded areas mark the NTP Stokes peaks while the blue dashed line highlights the peak with highest conversion efficiency. (b) The Raman conversion efficiencies of the Stokes peak at 1340 cm-1 with different incident angles. (c) The Raman conversion efficiencies at 1340 nm^{-1} for each measurement along z-direction with 75° illumination. (d) The dashed curve is the measured back-scattered Raman spectrum with the waveguide mode excitation. The solid curve is the spectrum obtained foe an oblique free-space excitation at an angle of 75°. The NTP Stokes peaks are highlighted by yellow shaded areas.

Raman background response associated to the silicon nitride is significantly reduced in the case of the free-space excitation.

VI. Conclusion

We report a novel on-chip approach for surface-enhanced Raman spectroscopy using a plasmonic slot waveguide. The molecules are excited by free-space oblique illumination in a nanoplasmonic structure designed to generate a resonant Electric field with a substantial enhancement. First, we have reported the field distributions of the excitation field at different incident angles. Then, we have experimentally confirmed our simulations by obtaining a high and reproducible Raman conversion efficiency ($\approx 1\times 10^{-11}$) when the waveguide is illuminated at 75° incidence. We also show this conversion could be improved further using optimized geometry lowering the height of the gap and shrinking its width [26], [27].

Our plasmonic structure is such that the excitation field overlaps poorly with the Si_3N_4 core therefore suppressing the spurious Raman contribution originating from it. As a result, the Raman background in the free-space case is up to an order of magnitude lower than that with waveguide-mode excitation. This has been verified experimentally via a comparison of waveguide excitation and oblique free space excitation. The result shows clearly the added value of the top illumination.

The excitation being from the top of the plasmonic structure and the collection being in the waveguide, a substantial resulting advantage is that the excitation beam couples eventually to the output port only very weakly (−50dB). As a direct consequence of this, the purity (side mode suppression) of the pumping laser source is of less importance than for any other Raman sensor. In the future, it will allow using cheaper laser diode sources and to bring the light to the sensor with a conventional optical fiber without worrying about the Raman scattering occurring in it. The improvement of signal-to-background ratio also greatly lifts the restrictions on the length of the waveguide between the edge and the Raman sensor, which will promote the integration of the Raman sensor with other components, such as spectral filters and spectrometers and pave the way for an on-chip Raman detection platform.

Acknowledgment

The authors acknowledge Prof. Nicolas Le Thomas for useful discussion. They also acknowledge Liesbet Van Landschoot for taking the SEM images.

REFERENCES

[1] J. X. Cheng and X. S. Xie, *Coherent Raman Scattering Microscopy*. New York, NY, USA: Taylor & Francis, 2012.

[2] C. Krafft, G. Steiner, C. Beleites, and R. Salzer, "Disease recognition by infrared and Raman spectroscopy," *J. Biophoton.*, vol. 2, nos. 1–2, pp. 13–28, Feb. 2009.

[3] B. Bao, J. Riordon, F. Mostowfi, and D. Sinton, "Microfluidic and nanofluidic phase behaviour characterization for industrial CO_2, oil and gas," *Lab Chip*, vol. 17, no. 16, pp. 2740–2759, 2017.

[4] J. R. Ferraro, K. Nakamoto, and C. W. Brown, *Introductory Raman Spectroscopy*, 2nd ed. Amsterdam, The Netherlands: Academic, 2003.

[5] D. Yan, J. Popp, M. W. Pletz, and T. Frosch, "Highly sensitive broadband Raman sensing of antibiotics in step-index hollow-core photonic crystal fibers," *ACS Photon.*, vol. 4, pp. 138–145, Jan. 2017.

[6] W. Xie, B. Walkenfort, and S. Schlücker, "Label-free SERS monitoring of chemical reactions catalyzed by small gold nanoparticles using 3D plasmonic superstructures," *J. Amer. Chem. Soc.*, vol. 135, no. 5, pp. 1657–1660, Nov. 2012.

[7] X.-M. Qian and S. M. Nie, "Single-molecule and single-nanoparticle SERS: From fundamental mechanisms to biomedical applications," *Chem. Soc. Rev.*, vol. 37, no. 5, pp. 912–920 2008.

[8] X. Hong, D. Wang, and Y. Li, "Kinked gold nanowires and their SPR/SERS properties," *Chem. Commun.*, vol. 47, no. 35, pp. 9909–9911, 2011.

[9] G. Das *et al.*, "Nano-patterned SERS substrate: Application for protein analysis vs. temperature," *Biosensors Bioelectron.*, vol. 24, no. 6, pp. 1693–1699, Feb. 2009.

[10] Y. Zhao *et al.*, "Constructing sensitive SERS substrate with a sandwich structure separated by single layer graphene," *Sens. Actuators B, Chem.*, vol. 263, pp. 634–642, Jun. 2018.

[11] Y. Zhao *et al.*, "Constructing sub-10-nm gaps in graphene-metal hybrid system for advanced surface-enhanced Raman scattering detection," *J. Alloys Compounds*, vol. 720, pp. 139–146, Oct. 2017.

[12] A. Dhakal, A. Z. Subramanian, P. Wuytens, F. Peyskens, N. L. Thomas, and R. Baets, "Evanescent excitation and collection of spontaneous Raman spectra using silicon nitride nanophotonic waveguides," *Opt. Lett.*, vol. 39, no. 13, pp. 4025–4028, Jul. 2014.

[13] A. Dhakal, P. C. Wuytens, F. Peyskens, K. Jans, N. L. Thomas, and R. Baets, "Nanophotonic waveguide enhanced Raman spectroscopy of biological submonolayers," *ACS Photon.*, vol. 3, no. 11, pp. 2141–2149, Nov. 2016.

[14] Y.-F. Xiao, Y.-C. Liu, B.-B. Li, Y.-L. Chen, Y. Li, and Q. Gong, "Strongly enhanced light-matter interaction in a hybrid photonic-plasmonic resonator," *Phys. Rev. A, Gen. Phys.*, vol. 85, Mar. 2012, Art. no. 31805.

[15] P. Vasa and C. Lienau, "Strong light–matter interaction in quantum emitter/metal hybrid nanostructures," *ACS Photon.*, vol. 5, pp. 2–23, Oct. 2018.

[16] J. A. Schuller, E. S. Barnard, W. Cai, Y. C. Jun, J. S. White, and M. L. Brongersma, "Plasmonics for extreme light concentration and manipulation," *Nature Mater.*, vol. 9, no. 3, pp. 193–204, Mar. 2010.

[17] S. Tanwar, K. K. Haldar, and T. Sen, "DNA origami directed Au nanostar dimers for single-molecule surface-enhanced Raman scattering," *J. Amer. Chem. Soc.*, vol. 139, pp. 17639–17648, Nov. 2017.

[18] A. Raza *et al.*, "High index contrast photonic platforms for on-chip Raman spectroscopy," *Opt. Exp.*, vol. 27, no. 16, pp. 23067–23079, Aug. 2019.

[19] N. Le Thomas, A. Dhakal, A. Raza, F. Peyskens, and R. Baets, "Impact of fundamental thermodynamic fluctuations on light propagating in photonic waveguides made of amorphous materials," *Optica*, vol. 5, no. 4, pp. 328–336, Mar. 2018.

[20] R. E. Bartolo, A. B. Tveten, and A. Dandridge, "Thermal phase noise measurements in optical fiber interferometers," *J. Quantum Electron.*, vol. 48, no. 5, pp. 720–727, May 2012.

[21] P. Measor *et al.*, "On-chip surface-enhanced Raman scattering detection using integrated liquid-core waveguides," *Appl. Phys. Lett*, vol. 90, May 2017, Art. no. 211107.

[22] L. Kong, C. Lee, C. M. Earhart, B. Cordovez, and J. W. Chan, "A nanotweezer system for evanescent wave excited surface enhanced Raman spectroscopy (SERS) of single nanoparticles," *Opt. Exp.*, vol. 23, no. 5, pp. 6793–6802, 2015.

[23] S. Lin, W. Zhu, Y. Jin, and K. B. Crozier, "Surface-enhanced Raman scattering with Ag nanoparticles optically trapped by a photonic crystal cavity," *Nano Lett.*, vol. 13, pp. 559–563, Jan. 2013.

[24] A. Raza *et al.*, "ALD assisted nanoplasmonic slot waveguide for on-chip enhanced Raman spectroscopy," *APL Photon.*, vol. 3, no. 11, Sep. 2018, Art. no. 116105.

[25] F. Peyskens, A. Dhakal, P. V. Dorpe, N. L. Thomas, and R. Baets, "Surface enhanced Raman spectroscopy using a single mode nanophotonic-plasmonic platform," *ACS Photon.*, vol. 3, pp. 102–108, Dec. 2016.

[26] D. Ji *et al.*, "Efficient mid-infrared light confinement within sub-5-nm gaps for extreme field enhancement," *Adv. Opt. Mater.*, vol. 5, Sep. 2017, Art. no. 1700223.

[27] X. Chen *et al.*, "Atomic layer lithography of wafer-scale nanogap arrays for extreme confinement of electromagnetic waves," *Nat. Commun*, vol. 4, Sep. 2013, Art. no. 2361.

Yang Li was born in Shandong, China, in 1992. She received the B.Sc. degree in information engineering from Zhejiang University, Hangzhou, China, in 2015. She is currently pursuing the joint Ph.D. degree with Zhejiang University and with the Photonics Research Group, Ghent University, Ghent, Belgium. She is currently involved in the surface-enhanced Raman spectroscopy on silicon nitride plasmonic slot waveguide.

Haolan Zhao received the B.Sc. degree in electrical engineering from Beihang University, Beijing, China, in 2011, and the M.Sc. degree in photonics and the Ph.D. degree from Ghent University, Ghent, Belgium, in 2013 and 2018, respectively. He is currently working on the development of integrated Raman sensors for volatile organic compound (VOC) monitoring. His research interest includes the implementation of coherent Raman scattering based on the silicon nitride platform.

Ali Raza received the B.S. degree in engineering sciences (photonics engineering) from GIKI, Pakistan, and the M.Sc. degree in photonics sciences from UEF, Finland, in 2015. He is currently pursuing the Ph.D. degree with the Photonics Research Group, Ghent University, Belgium. He is working on waveguide-enhanced and surface-enhanced Raman spectroscopy on a hybrid SiN-plasmonics platform. While pursuing the B.S. degree, he did research internships at British American Tobacco (BAT) and Attock oil refinery. While pursuing the master's degree, he also did a research internship at DESY, Hamburg, Germany.

Stéphane Clemmen received the M.Sc. degree in physics and the Ph.D. degree from the Université Libre de Bruxelles (ULB) in 2006 and 2010, respectively. He is currently a Professor with Ghent University and an FNRS Researcher with ULB. He held a post-doctoral position at Cornell University, Ithaca, NY, USA, from 2010 to 2014, and at Ghent University from 2014 to 2017. He works mainly on quantum photonics, nonlinear optics, and Raman spectroscopy.

Roel Baets (M'88–SM'96–F'07) received the first M.Sc. degree in electrical engineering from Ghent University (UGent) in 1980, the second M.Sc. degree from Stanford University in 1981, and the Ph.D. degree from UGent in 1984.

From 1984 to 1989, he held a post-doctoral position at IMEC. Since 1989, he has been a Professor with the Faculty of Engineering and Architecture, UGent, where he founded the Photonics Research Group. From 1990 to 1994, he was a part-time Professor with the Delft University of Technology and from 2004 to 2008 with the Eindhoven University of Technology. He is currently a Full Professor with UGent and is associated with IMEC. He has mainly worked in the field of integrated photonics. He has made contributions to research on photonic integrated circuits, both in III–V semiconductors and in silicon, as well as their applications in telecom, datacom, sensing, and medicine.

Dr. Baets is an ERC Grantee of the European Research Council and a Methusalem Grantee of the Flemish Government. He is a fellow of the European Optical Society (EOS) and the Optical Society (OSA). He is also a member of the Royal Flemish Academy of Belgium for Science and the Arts.